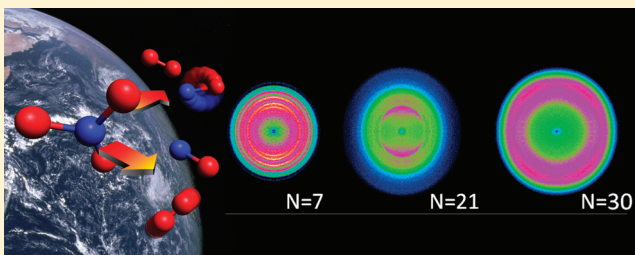


# Ion Imaging Study of NO<sub>3</sub> Radical Photodissociation Dynamics: Characterization of Multiple Reaction Pathways

Michael P. Grubb, Michelle L. Warter, Kurt M. Johnson, and Simon W. North\*

Department of Chemistry, Texas A&amp;M University, College Station, Texas 77842, United States

**ABSTRACT:** The photodissociation of NO<sub>3</sub> has been studied using velocity map ion imaging. Measurements of the NO<sub>2</sub> + O channel reveal statistical branching ratios of the O(<sup>3</sup>P<sub>J</sub>) fine-structure states, isotropic angular distributions, and low product translational energy consistent with barrierless dissociation along the ground state potential surface. There is clear evidence for two distinct pathways to the formation of NO + O<sub>2</sub> products. The dominant pathway (>70% yield) is characterized by vibrationally excited O<sub>2</sub>(<sup>3</sup>Σ<sub>g</sub><sup>−</sup>, ν = 5–10) and rotationally cold NO(<sup>2</sup>Π), while the second pathway is characterized by O<sub>2</sub>(<sup>3</sup>Σ<sub>g</sub><sup>−</sup>, ν = 0–4) and rotationally hotter NO(<sup>2</sup>Π) fragments. We speculate the first pathway has many similarities to the “roaming” dynamics recently implicated in several systems. The rotational angular momentum of the molecular fragments is positively correlated for this channel, suggesting geometric constraints in the dissociation. The second pathway results in almost exclusive formation of NO(<sup>2</sup>Π, ν = 0). Although product state correlations support dissociation via an as yet unidentified three-center transition state, theoretical confirmation is needed.



## INTRODUCTION

The nitrate radical, NO<sub>3</sub>, is an important intermediate in both stratospheric and tropospheric chemical cycles. Photolysis in the visible region yields two product channels with the indicated wavelength thresholds at 0 K:<sup>1</sup>



Channel 2 plays a well-established role in the catalytic destruction of ozone, and thus the branching ratio of the two channels as a function of visible wavelength has been well established.<sup>1–3</sup> The quantum yield of channel 1 above its 585.5 nm threshold is close to unity due to the large difference in the unimolecular rates of the two channels. Since channel 1 is presumed to occur via a loose transition state, the dissociation process for channel 1 is orders of magnitude faster (<10<sup>−11</sup> s) than channel 2 (≈10<sup>−9</sup> s), which is presumed to involve a tighter transition state.<sup>4</sup> Despite the narrow energetic window, channel 2 accounts for about 11% of the atmospheric photoproducts.<sup>5</sup> However, a molecular level description for dissociation via channel 2 is still unknown as no transition state of relevant energy has yet been identified by experiment or theory.

There are three low-lying electronic states relevant to the visible photolysis of NO<sub>3</sub> (Figure 1): X <sup>2</sup>A', A <sup>2</sup>E'', and B <sup>2</sup>E'. Excitation to A <sup>2</sup>E'' is symmetry forbidden, and cavity ringdown absorption spectroscopy and theoretical calculations of the NO<sub>3</sub>(A <sup>2</sup>E'') ← NO<sub>3</sub>(X <sup>2</sup>A') transition have revealed complex intensity borrowing.<sup>6</sup> There have been extensive spectroscopic

studies of the strong NO<sub>3</sub>(B <sup>2</sup>E') ← NO<sub>3</sub>(X <sup>2</sup>A') transition used as the spectroscopic probe for NO<sub>3</sub> in the atmosphere. The high resolution absorption spectrum reported by Marinelli et al. revealed diffuse bands with unresolved rotational structure, indicating that the NO<sub>3</sub>(B <sup>2</sup>E') state is short-lived.<sup>7</sup> The long microsecond fluorescence lifetimes (300 × 10<sup>−6</sup> s)<sup>8</sup> found by Nelson et al. indicate strong vibronic coupling of the NO<sub>3</sub>(B <sup>2</sup>E') state to the nonemitting dense manifold of states in the NO<sub>3</sub>(X <sup>2</sup>A') ground state.<sup>8</sup> Picosecond pump–probe measurements by Wittig and co-workers of the NO fragment arising from channel 2 yielded unimolecular dissociation rates consistent with rapid internal conversion, although the authors could not rule out the possibility of participation of the NO<sub>3</sub>(A <sup>2</sup>E'') state.<sup>4,9</sup> However, it is currently believed that NO<sub>3</sub> dissociation along channel 2 occurs along the ground state potential and that the barrier originates from an avoided crossing of the NO<sub>3</sub>(X <sup>2</sup>A') state with an excited repulsive state correlating to the NO + O<sub>2</sub> fragments.

There have been several experimental studies of NO<sub>3</sub> photolysis focused on understanding the underlying dynamics of the two channels through measurement and analysis of the product state distributions. The total translational energy distributions associated with channel 1 revealed statistical energy partitioning, consistent with a barrierless reaction.<sup>1</sup> Although there was speculation that the dissociation could partially occur on the NO<sub>3</sub>(B <sup>2</sup>E') surface, theoretical calculations of the potential

Received: January 5, 2011

Revised: February 22, 2011

Published: March 29, 2011

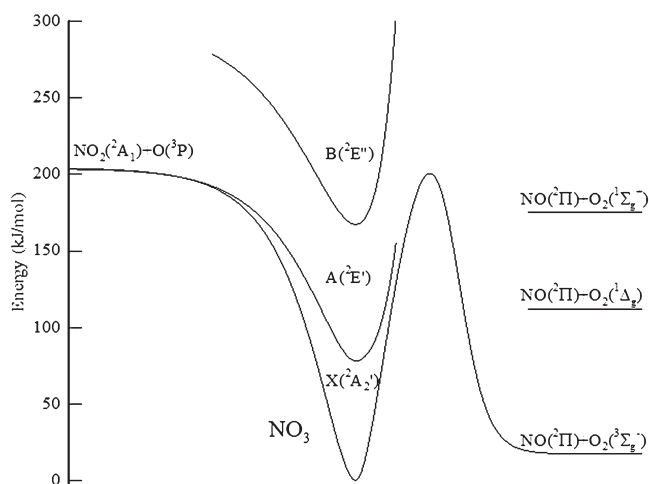
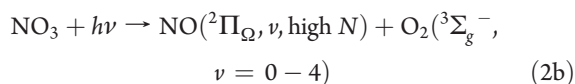
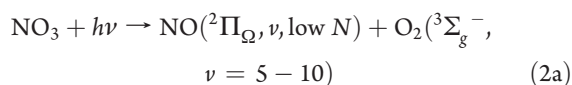


**Figure 1.** Schematic energy diagram for the dissociation channels in  $\text{NO}_3$ .

energy surfaces leading to channel 1 by Eisfeld and Morokuma found that the  $\text{NO}_3(\text{B } ^2\text{E}')$  state is not adiabatically correlated to ground state  $\text{NO}_2(^2\text{A}_1) + \text{O}(^3\text{P})$  products, suggesting that channel 1 should proceed via the ground  $\text{NO}_3(\text{X } ^2\text{A}_1')$  state.<sup>10</sup>

The total translational energy distributions associated with channel 2 revealed the presence of highly excited  $\text{O}_2$  products, although it was unclear whether the excitation was electronic  $\text{O}_2(^1\Delta_g)$  or vibrational  $\text{O}_2(^3\Sigma_g^-, \nu = 5-10)$ .<sup>1</sup> State-selective experiments conducted by Mikhaylichenko et al. confirmed the presence of excited  $\text{O}_2$  products and measured a nascent NO rotational temperature of  $1400 \pm 300$  K with low vibrational energy.<sup>9</sup> Recently, we reported the results of high resolution velocity map ion imaging studies of channel 2 which clearly indicate that the fragments are formed in the electronic ground state of  $\text{O}_2$ .<sup>11</sup> Additionally, we demonstrated that channel 2 is produced through two pathways with distinct correlated product distributions:



The first pathway, channel 2a, yields vibrationally excited  $\text{O}_2(^3\Sigma_g^-, \nu = 5-10)$  correlated with the lower rotational levels of  $\text{NO}(^2\Pi)$ . The second pathway, channel 2b, yields vibrationally colder  $\text{O}_2(^3\Sigma_g^-, \nu = 0-4)$  fragments correlated with the higher rotational levels of  $\text{NO}(^2\Pi)$ . In this paper we present a more detailed experimental analysis of the products resulting from these channels, as well as the dynamic implications of the results. We discuss the results in the context of similarities to the recently discussed “roaming” mechanism of formaldehyde and other systems.<sup>12,13</sup>

Roaming in photodissociation dynamics has been a subject of considerable recent interest.<sup>14</sup> The roaming mechanism is characterized by large amplitude motion associated with a frustrated radical dissociation, which leads to intramolecular abstraction dynamics. In formaldehyde dissociation at excitation energies near the  $\text{HCO} + \text{H}$  radical threshold, calculations reveal trajectories where a C–H bond initially stretches to long bond

distances where the H atom orbits the HCO, sampling a large region of the potential energy surface before eventually abstracting the other H atom to form the  $\text{CO} + \text{H}_2$  products.<sup>15</sup> These trajectories give rise to vibrationally excited  $\text{H}_2$  due to the extended bond lengths at which it is formed. Since roaming can be thought of as an *intramolecular* abstraction, the result is product distributions nearly identical to the related *intermolecular* abstraction.<sup>16</sup> Although roaming dynamics were first speculated to occur only for hydrogen atoms, roaming has since been proposed in the photodissociation of acetaldehyde, acetone, and various alkanes.<sup>17–19</sup>

## EXPERIMENTAL SECTION

The molecular beam/velocity map ion imaging apparatus has been described in detail elsewhere.<sup>20,21</sup> The molecular beam of  $\text{NO}_3$  was made from flash pyrolysis of  $\text{N}_2\text{O}_5$  in a heated source (650–750 K) controlled by a current-regulated power supply.<sup>22</sup> The  $\text{NO}_3$  precursor,  $\text{N}_2\text{O}_5$ , was synthesized by flowing excess ozone over the  $\text{NO}_2$  at  $-60$  °C. The resulting  $\text{N}_2\text{O}_5$  was slowly trapped in a second bubbler at  $-78$  °C as a white solid.<sup>23</sup> The  $\text{N}_2\text{O}_5$  was kept at approximately  $-10$  °C during the experiment in an acetone bath, to generate a 1%  $\text{N}_2\text{O}_5$  gas mixture in 800 Torr of helium. The observed signal distribution was found to be independent of  $\text{N}_2\text{O}_5$  partial pressures ranging from 0.4 to 2%. The pulsed (General Valve Series 9) free jet expansion was collimated by a conical skimmer before entering the imaging region of the apparatus. The expansion-cooled  $\text{NO}_3$  beam was then intersected at  $90^\circ$  by the output of two linearly polarized pulsed dye lasers. The photolysis beam was generated by a Spectra Physics GCR-150-10 Nd:YAG (532 nm) pumped dye laser (PDL) with wavelengths ranging from 583 to 595 nm. The dissociation wavelengths were accurately determined by optogalvanic calibration using a Cu–Ne hollow cathode lamp. The probe beam was generated by the third harmonic of a second Nd:YAG laser (355 nm) which pumped an LAS dye laser to generate 450–470 nm. The dye laser output was frequency doubled to generate wavelengths corresponding to 1 + 1 REMPI transitions of NO through the A–X (0,0) band (224–226 nm) and the A–X (0,1) band (234–237 nm).<sup>24</sup> Typical photolysis and probe pulse energies were 500 and 100  $\mu\text{J}/\text{pulse}$ , respectively. A pump–probe delay time used for the experiment was typically  $\sim 25$  ns, and longer delay times of over 100 ns did not alter the signal distribution. The resulting cations were accelerated down a 50 cm time-of-flight tube by electrostatic lenses before striking a position-sensitive MCP/phosphor screen detector. A gated CCD camera captured the resulting signal. The accumulated images were reconstructed using the polar onion peeling algorithm developed by Roberts et al. to obtain radial and angular distributions.<sup>25</sup> Transformation of the radial distributions to speed distributions was performed using an experimentally determined speed/pixel conversion factor. We have chosen to transform the speed distributions to center-of-mass total translational energy distributions for comparison to simulations.

The  $\text{NO}_3$  signal was dependent on the source temperature and photolysis wavelength, and was not present at ambient nozzle temperatures or when the photolysis laser was blocked. The translational energy distribution was found to be independent of the power of either laser, and the overall signal was found to be linearly dependent on the photolysis power. In addition, the intensity of the signal associated with both dissociation channels

**Table 1.** Experimental and Statistical Branching Ratios of  $O(^3P_J)$  Products Resulting from Channel 1 at 583 nm

	experimental	statistical
$O(^3P_2)$	$0.54 \pm 0.05$	0.55
$O(^3P_1)$	$0.38 \pm 0.08$	0.33
$O(^3P_0)$	$0.08 \pm 0.03$	0.11

exhibited wavelength dependences consistent with previous quantum yield measurements.

## RESULTS AND DISCUSSION

**Atomic Elimination Channel:**  $NO_3 \rightarrow O(^3P) + NO_2$ . Images of the  $O(^3P_J)$  fragments originating from the  $O(^3P_J) + NO_2$  radical channel were obtained at wavelengths between 582 and 598 nm, both above and below the 0 K channel thresholds. All the measured images were isotropic ( $\beta = 0.1 \pm 0.2$ ), consistent with the lifetimes reported by Davis et al. which exceed the parent rotational period.<sup>4</sup> The branching between the three spin–orbit states of oxygen as a function of wavelength was found by integrating the total image signal of each selectively ionized spin–orbit state and subtracting the background  $NO_2$  signal from probe beam dissociation. The results for photodissociation at 583 nm are presented in Table 1. The experimental fine structure branching ratios are very close to the statistical prediction, as expected for a barrierless dissociation on the ground state potential energy surface.

The  $P(E_T)$  distributions derived from  $O(^3P_2)$  images were not sensitive to photolysis wavelength over the range from 582 to 598 nm, and we observed no significant difference between the  $O(^3P_J)$  images at a given wavelength. The distributions measured at 584, 590, and 598 nm are shown in Figure 2 (filled circles) and are all broad and peak near zero translational energy as expected for barrierless dissociation.<sup>26</sup> The results are in good agreement with the state-averaged distributions reported by Davis et al.,<sup>1</sup> which is not surprising given the similarity between the  $P(E_T)$  distributions associated with each oxygen fine-structure state. We have modeled the  $P(E_T)$  distributions using a prior distribution,<sup>27,28</sup> suitable for describing statistical energy partitioning, to further characterize the initial parent  $NO_3$  energy distribution. The  $P(E_T)$  distributions were of the following form::

$$P(f_T) = (f_T)^{1/2}(1 - f_T)^{7/2} \quad (3)$$

where  $f_T$  is the fraction of the available energy in translation.<sup>27</sup> Distributions for each rovibrational state of the parent  $NO_3$  were weighted according to assumed Boltzmann temperatures for both rotation and vibration. We find that the final distributions are sensitive to the parent internal energy, as measurements lying below the 0 K channel threshold necessarily arise from the dissociation of rotationally and vibrationally excited parent molecules. Prior distributions assuming an  $NO_3$  rotational temperature of 20 K and vibrational temperature of 300 K provide a satisfactory fit to the data and are shown as the solid lines in Figure 2. Lowering the parent vibrational distribution to 100 K (dashed line) results in a colder  $P(E_T)$  distribution than observed. This finding is not unexpected given the heated source and the higher efficiency for rotational cooling relative to vibrational cooling in the jet expansion. It should be noted that this model was less sensitive to changes in the rotational temperature, the characterization of which is discussed later within this paper.

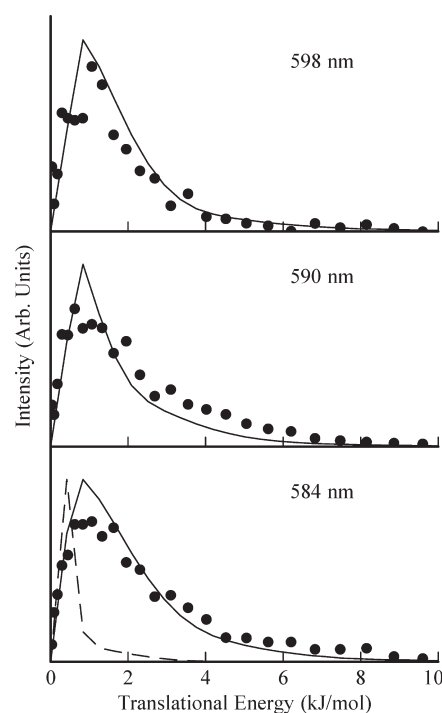


**Figure 2.** Total translational energy distributions of  $O(^3P_2)$  resulting from channel 1 at three pump wavelengths (symbols). Also shown are simulated prior distributions assuming a parent  $NO_3$  rotational temperature of 20 K and vibrational temperatures of 300 K (solid line) and 100 K (dashed line).

**Molecular Channel:**  $NO_3 \rightarrow NO + O_2$ . Velocity map ion images of the  $NO(^2\Pi_{\Omega}, v = 0, N)$  arising from  $NO_3$  dissociation at 588 nm are shown in Figure 3. The angular distributions associated with the images were isotropic,<sup>29</sup> consistent with a dissociation lifetime longer than the parent rotational period in agreement with the previous experimental measurements of the unimolecular dissociation rates.<sup>4</sup> The highly anisotropic feature, clearly evident in the  $N = 7$  and  $N = 21$  images, corresponds to the photodissociation of  $NO_2$  at the 226 nm probe wavelength.<sup>30</sup>

The total translational energy distributions, or  $P(E_T)$  distributions, derived from specific  $NO(^2\Pi_{\Omega}, v = 0, N)$  state images are shown as the filled symbols in Figure 4. Forward convolution simulations to the data are shown as solid lines. The total translational energy for a given set of coincident product final states is given by

$$E_T = h \frac{c}{\lambda} - \Delta H_{rxn} + E_{NO_3}(T_e, v, N) - E_{NO}(T_e, v, N) - E_{O_2}(T_e, v, N) \quad (4)$$

where  $\lambda$  is the photolysis wavelength,  $\Delta H_{rxn}$  is the asymptotic energy of the  $NO + O_2$  channel ( $\sim 12.5$  kJ/mol), and  $E_{NO}$  and  $E_{O_2}$  are the internal energies of the product fragments. The internal energy of the parent  $NO_3$  molecule can be neglected based on experimental measurements (vide infra). The internal energy of the fragments was calculated using known spectroscopic data.<sup>31</sup> The internal energy of the NO fragment is state specified by the 1 + 1 REMPI process for the total  $P(E_T)$  distributions derived from the NO images. In the forward convolution fitting procedure, an assumed coincident  $O_2$  rovibrational distribution and instrument response function are used to generate the total  $P(E_T)$  using eq 4.



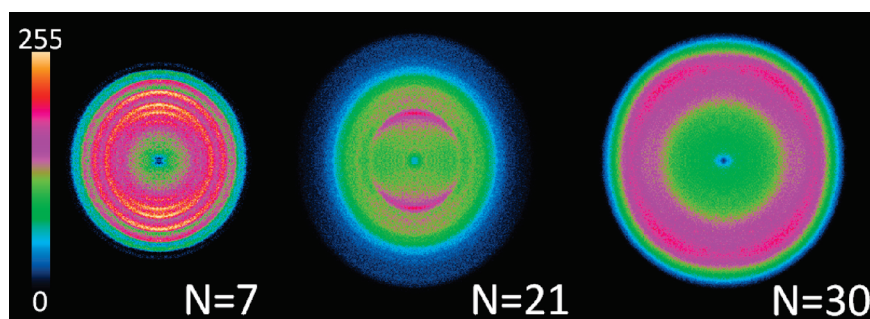


Figure 3. Ion images of  $\text{NO}(^2\Pi, \nu = 0, N)$  fragments arising from the dissociation of  $\text{NO}_3$  at 588 nm.

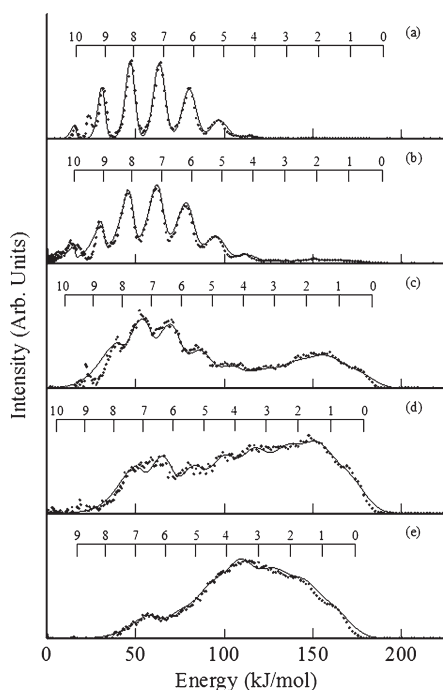


Figure 4. Translational energy distributions of specific rotational states of  $\text{NO}(^2\Pi)$ : (a)  $N = 7$ , (b)  $N = 13$ , (c)  $N = 21$ , (d)  $N = 26$ , and (e)  $N = 30$  (symbols). Forward convolution fits to the data are shown as solid lines.

Based on simulations to the  $P(E_T)$  distributions, we find that the low translational energy signal must originate from vibrational excitation of  $\text{O}_2(^3\Sigma_g^-)$  fragments. Attempts to model the structure of the  $\text{NO}(^2\Pi_\Omega, \nu = 0, N = 7)$   $P(E_T)$  assuming significant  $\text{O}_2(^1\Delta_g)$  cofragments were inconsistent with the data. The previous state-averaged measurements of Davis et al.<sup>1</sup> and the lower resolution pump–probe measurements of Mikhaylichenko et al.<sup>9</sup> were unable to discount the formation of  $\text{O}_2(^1\Delta_g)$  in the dissociation. The combs above the distributions in Figure 4 correspond to the energetic limits associated with  $\text{O}_2(^3\Sigma_g^-)$  vibrational states. The  $P(E_T)$  distributions were modeled assuming a Gaussian rotational distribution for each  $\text{O}_2(^3\Sigma_g^-)$  vibrational band of variable intensity. The peak of the rotational distributions varied from  $N_{\text{max}} = 11$  coincident with  $\text{NO}(^2\Pi_\Omega, \nu = 0, N = 7)$  to  $N_{\text{max}} = 29$  coincident with  $\text{NO}(^2\Pi_\Omega, \nu = 0, N = 30)$  with full width at half-maximum widths varying from  $\Delta N = 12$  to  $\Delta N = 28$  over this same range. A single  $\text{O}_2$  rotational distribution was employed for every  $\text{O}_2$  vibrational band coincident with a specific  $\text{NO}(^2\Pi_\Omega, \nu = 0, N)$

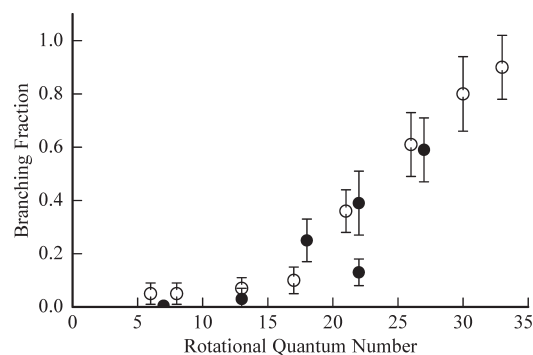
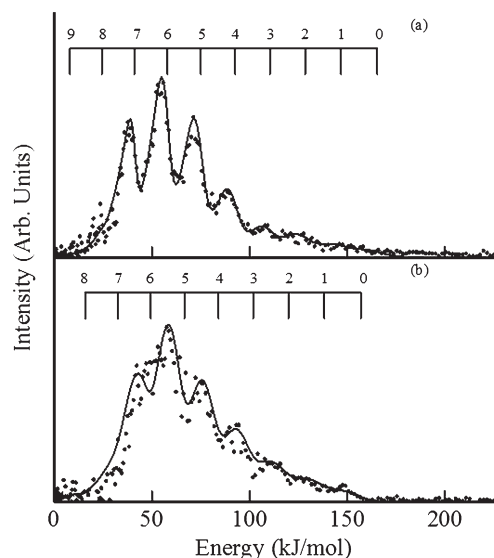


Figure 5. Branching fraction of channel 2b as a function of NO rotational state for  $\text{NO}(^2\Pi_{3/2})$  (filled circles) and  $\text{NO}(^2\Pi_{1/2})$  (open circles).

state. Both the  $N_{\text{max}}$  and  $\Delta N$  parameters describing the  $\text{O}_2$  rotational distributions showed an increasing trend with increased NO rotation, indicating a positive correlation in the angular momentum of both fragments. Further parametrization was not required to provide reasonable fits to the experimental distributions, although there is evidence that the rotational distributions vary with  $\text{O}_2$  vibration for each detected NO state. For the highest NO rotational states individual  $\text{O}_2$  vibrational contributions are unresolved, and therefore the continued use of Gaussian rotational distributions is driven by convenience since alternative choices would likely still provide reasonable fits to the experimental distributions. The partitioning between  $\text{O}_2$  vibrational and rotational excitation is therefore less certain. The sharp features near 25 kJ/mol that are not fit by the simulations are due to NO arising from  $\text{NO}_2$  photodissociation by the probe laser.

The  $P(E_T)$  distributions derived from the reconstructed images exhibit strong evidence of two distinct product channels. One channel (2a), formed in coincidence with lower rotational states of  $\text{NO}(^2\Pi_\Omega)$ , results in vibrationally excited  $\text{O}_2(^3\Sigma_g^-)$  fragments ( $\nu = 5-10$ ). The  $P(E_T)$  distribution associated with  $\text{NO}(^2\Pi_{1/2}, \nu = 0, N = 7)$  in the top panel of Figure 2 shows very narrow peaks corresponding to low  $\text{O}_2$  rotational excitation. A second feature begins to emerge in  $P(E_T)$  distributions associated with higher detected NO rotational states. Although the vibrational structure in this channel is not well-resolved in any image, conservation of energy dictates that the signal must correspond to  $\text{O}_2(^3\Sigma_g^-)$  fragments.

The branching fraction of this second channel (2b) as a function of  $\text{NO}(^2\Pi_{1/2}, \nu = 0, N)$  and  $\text{NO}(^2\Pi_{3/2}, \nu = 0, N)$  is shown in Figure 5 and ranges from  $0.0 \pm 0.05$  for  $\text{NO}(N = 7)$  to above  $0.85 \pm 0.15$  for  $\text{NO}(N = 33)$ . These branching fractions



**Figure 6.** Translational energy distributions of  $\text{NO}(^2\Pi, \nu = 1)$ : (a)  $N = 15$  and (b)  $N = 24$  (filled circles). Forward convolution fits are shown as solid lines.

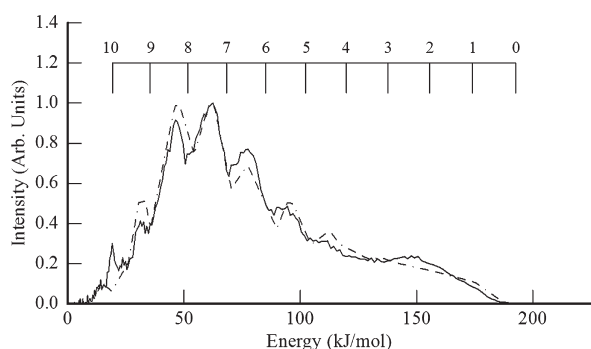


**Figure 7.** State-averaged total translational energy distribution assuming a NO rotational temperature of 1300 K, a 2:1 ratio of the  $\text{NO}(^2\Pi_{1/2}): \text{NO}(^2\Pi_{3/2})$ , and 10%  $\text{NO}(\nu = 1)$  (solid line), compared to the distribution reported by Davis et al. in ref 1 (dashed line).

were estimated assuming the correlated  $\text{O}_2$  vibrational distribution of each channel was equivalent for each NO state, although subtle differences in these distributions were in fact observed. This assumption, however, was necessary because the loss of structure in the highest NO  $N$ -state  $P(E_T)$  distributions precluded a unique decomposition into the two channels. The branching of the two channels with NO rotational state was independent of the final spin–orbit state, although images associated with the  $\text{NO}(^2\Pi_{3/2}, \nu = 0, N = 22)$  state, detected via the P2 branch, indicated an underpopulation of channel 2b relative to the trend of the other states. We have no explanation for this apparent anomaly at this time.

Images of  $\text{NO}(^2\Pi_{\Omega}, \nu = 1, N)$  fragments were also obtained via the A–X (0, 1) band near 235 nm. Figure 6 shows the  $P(E_T)$  distributions derived from  $N = 15$  and  $N = 24$  images. We observe an underpopulation of coincident  $\text{O}_2$  in low vibrational states (channel 2b) regardless of the rotational energy or spin–orbit state of the detected NO fragment. This observation indicates that channel 2b is associated with vibrationally colder NO fragments. Since the overall  $\text{NO}(\nu = 0):\text{NO}(\nu = 1)$  branching

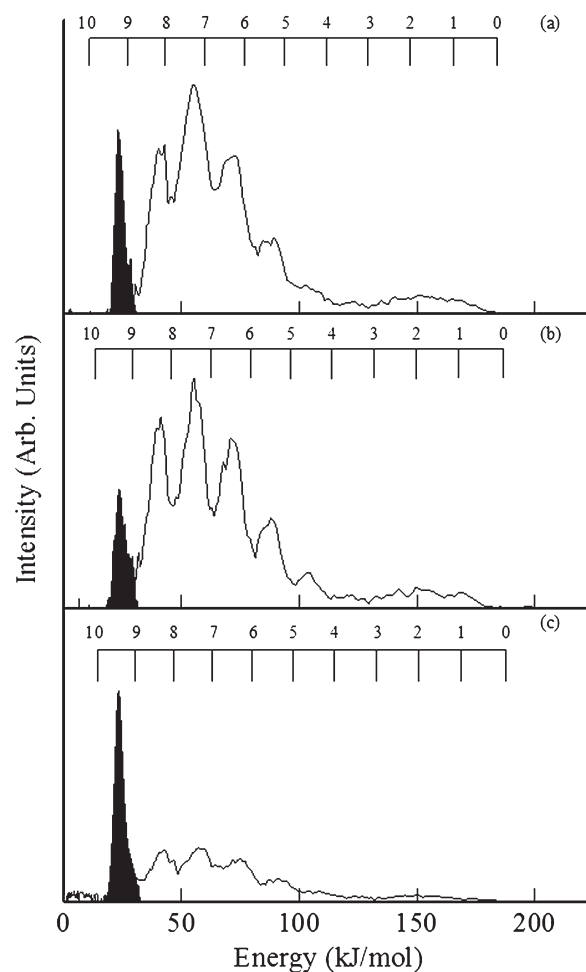


**Figure 8.** Total translational energy distribution derived from  $\text{NO}(^2\Pi_{1/2}, \nu = 0)$  at different pump wavelengths: (a) 595, (b) 588, and (c) 585 nm. The feature near 25 kJ/mol is due to  $\text{NO}_2$  photodissociation at 226 nm.

is 0.9:0.1 based on the measurements of Mikhaylichenko et al.,<sup>9</sup> NO fragments produced in 2b must be almost entirely in the vibrational ground state. Forward convolution simulations to the  $\text{NO}(\nu = 1)$  data reveal that the rotational energy of the  $\text{O}_2$  fragment is still positively correlated with the rotational energy of the NO fragment. Although the  $P(E_T)$  distributions associated with  $\text{NO}(\nu = 1)$  fragments are energetically similar to the distributions of the  $\text{NO}(\nu = 0)$  images, the available energy is decreased by the NO vibrational energy ( $\sim 23$  kJ/mol). Therefore, the  $\text{O}_2$  vibrational distributions are shifted by one quantum ( $\sim 19$  kJ/mol) relative to the  $\text{NO}(^2\Pi_{\Omega}, \nu = 0, N)$  results.

In order to compare the present state-selected imaging results to the state-averaged results reported by Davis et al.,<sup>1</sup> each  $\text{NO}(^2\Pi_{\Omega}, \nu, N)$   $P(E_T)$  distribution was weighted according to the state population and then summed. Distributions of both spin–orbit states were weighted using a 2:1 ratio of the  $\text{NO}(^2\Pi_{1/2})$  to  $\text{NO}(^2\Pi_{3/2})$  states, and the  $\text{NO}(^2\Pi_{\Omega}, \nu = 0)$  and  $\text{NO}(^2\Pi_{\Omega}, \nu = 1)$  distributions were weighted using a 9:1 ratio as reported by Mikhaylichenko et al.<sup>9</sup> The resultant weighted distribution is shown in Figure 7. The  $P(E_T)$  reported by Davis et al. is also provided for comparison. We find that the best agreement was achieved using an NO rotational temperature of 1300 K, consistent with the  $1400 \pm 300$  K rotational temperature determined by Mikhaylichenko et al.<sup>9</sup> The excellent

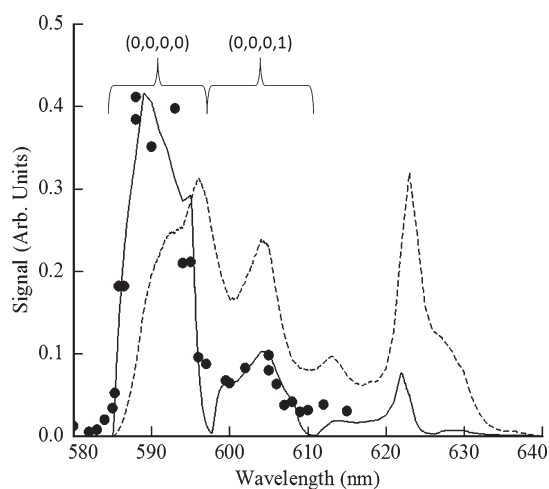


**Figure 9.** Relative experimental yields for the  $\text{NO} + \text{O}_2$  channel at a series of experimental wavelengths (filled symbols). Simulated yields of the  $\text{NO} + \text{O}_2$  channel with 20 K rotational and 300 K vibrational temperatures and 300 K rotational and 300 K vibrational temperatures are shown as solid and dashed lines, respectively.

agreement between the two distributions in Figure 7 suggests that the state-selected images result from a single photon dissociation at the photolysis wavelength and that dissociation due to the focused probe is not significant. An interesting observation, noted previously by Davis et al., is that the state-averaged  $P(E_T)$  from channel 2 exhibits both a vibrationally resolved region and an unresolved region at higher energy. The state-specific imaging measurements reveal that these two regions are a consequence of two distinct dissociation pathways.

The measured translational energy distributions of specific NO states were found to be independent of the photolysis wavelength over the 585–595 nm range, except for the expected shifts due to the small changes in available energy. As previously noted, this range of wavelengths corresponds to only 3 kJ/mol ( $258 \text{ cm}^{-1}$ ) in energy and the product energy partitioning is dominated by the large exit barrier for this channel. In addition,  $\text{NO}_3$  parent molecules with a single quantum of vibrational energy ( $363 \text{ cm}^{-1}$ ) would have enough energy to dissociate exclusively via the atomic elimination channel.  $P(E_T)$  distributions from  $\text{NO}(^2\Pi_{1/2}, v=0, N=17)$  at 585, 588, and 595 nm are shown in Figure 8. The feature associated with the 225 nm photodissociation of background  $\text{NO}_2$  has intentionally not been subtracted from these distributions to illustrate the relative change in the  $\text{NO} + \text{O}_2$  channel at different photolysis wavelengths since the  $\text{NO}_2$  contribution is only dependent on the fixed probe laser. Figure 9 shows the signal relative to the probe-induced dissociation of  $\text{NO}_2$  as a function of wavelength. As expected, the contribution from the  $\text{NO} + \text{O}_2$  channel decreases sharply at 585 nm, the radical channel threshold, and exhibits a maximum near 588 nm which was also observed by Davis et al.<sup>1</sup> corresponding to a maximum in the  $\text{NO}_3$  absorption cross section.

The relative intensities of the  $\text{NO}_2$  background signal and the  $\text{NO}_3$  signal at different wavelengths can be used to estimate the temperature of the parent  $\text{NO}_3$  molecules in the molecular beam based on the model of Johnston et al.<sup>5</sup> The solid line in Figure 9 shows the expected photolysis yield of the molecular product channel assuming  $\text{NO}_3$  rotational temperatures of 20 K, and the dashed line corresponds to an  $\text{NO}_3$  rotational temperature of 300 K. A comparison between the

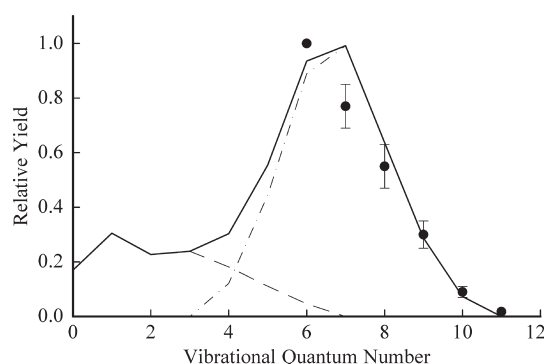


**Figure 10.** Total  $\text{O}_2$  vibrational distribution from  $\text{NO}_3$  dissociation at 588 nm (solid line) compared to LIF measurements arising from the  $\text{O}(^3\text{P}) + \text{NO}_2 \rightarrow \text{NO} + \text{O}_2$  reaction reported in ref 32 (symbols). Also shown are the approximate state-averaged vibrational distributions of channels 2a and 2b separately.

experimental results and the model suggests that the  $\text{NO}_3$  is rotationally cold. In both models the  $\text{NO}_3$  vibrational temperature is 300 K. The vibrational state of  $\text{NO}_3$  from which the signal originates is labeled on Figure 9, and shows that the signal at the measured wavelengths originates from either the vibrational ground state or with a single excitation of the degenerate  $\omega_4$  frequency mode ( $363 \text{ cm}^{-1}$ ). The best fit results are consistent with the parent internal energy derived from an analysis of the  $\text{NO}_2 + \text{O } P(E_T)$  distributions.

**Dynamics of the Molecular Elimination Channel.** Although the wavelength-dependent quantum yield for the formation of  $\text{NO} + \text{O}_2(^3\Sigma_g^-)$  in  $\text{NO}_3$  photolysis is well established, a molecular level description of the process remains uncertain. To our knowledge no three-center transition state on the ground potential energy surface of *relevant energy* has been identified for this system. Our state-selected NO images suggest that there are two independent pathways leading to  $\text{NO} + \text{O}_2(^3\Sigma_g^-)$  products. On the basis of the overall and correlated scalar distributions, we postulate that one pathway (2a) has many characteristics associated with a roaming-type mechanism discussed extensively in the case of formaldehyde dissociation. The origin of the second pathway (2b) is less clear, but our measurements suggest a similarity to dynamics via a tight transition state and provide important constraints for future theoretical studies. Interestingly, if these descriptions are indeed correct, it suggests that the roaming mechanism is the dominant molecular dissociation mechanism, accounting for >70% of the products. The invariance of the state-selected images with photolysis wavelength indicates that the branching between channels 2a and 2b is wavelength independent. This differs from the behavior in formaldehyde, where a clear increase in the branching ratio of the roaming channel relative to the transition state channel was observed with decreasing photolysis wavelength. In  $\text{NO}_3$  this is most likely due to the narrow window available to the molecular channel, a result of the abrupt closure of the channel once the  $\text{NO}_2 + \text{O}$  channel becomes energetically accessible.

The NO state-dependent  $\text{O}_2$  vibrational distributions provide the clearest evidence of these two channels in analogy to the  $\text{H}_2$  vibrational/ $\text{CO}$  rotational correlations in formaldehyde.<sup>12</sup> At low NO rotational states the coincident  $\text{O}_2$  is found in high vibrational states, peaking near  $v=7$ . Although the coincident  $\text{O}_2$  vibrational distribution exhibits a slight negative correlation with NO rotational state, the distribution for this channel remains approximately constant. The second channel is characterized by

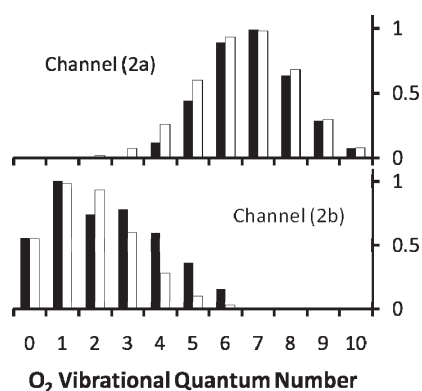


**Figure 11.** Estimated state-averaged  $O_2$  vibrational distributions for the molecular product channels (black bars) and Franck–Condon simulations assuming O–O bond distances of 1.451 (2a) and 1.320 Å (2b), respectively (white bars).

higher NO rotational states and lower  $O_2$  vibrational states. Figure 10 shows the NO state-averaged total  $O_2$  vibrational distribution associated with these two channels (dashed lines). The decomposition into two channels is supported by the fits to the experimental  $P(E_T)$  distributions. Recent trajectory calculations by Christoffel et al. predicted similar  $H_2$  vibrational distributions arising from unimolecular roaming and the direct  $H + HCO$  abstraction reaction.<sup>16</sup> Thus, the  $O_2$  produced as a result of oxygen atom roaming, or large amplitude motion, should resemble the dynamics of direct oxygen atom abstraction from  $NO_2$ . Although the  $O + NO_2$  reaction proceeds via both a direct (60%) and a complex-forming mechanism (40%),<sup>33</sup> we predict that >70% of the complexes will follow a roaming mechanism. Therefore, a comparison with the bimolecular results should be instructive.<sup>16</sup> Smith et al. reported laser induced fluorescence (LIF) measurements of the nascent  $O_2$  vibrational distribution of the thermal  $NO_2 + O \rightarrow NO + O_2$  reaction.<sup>32</sup> Due to diminishing Franck–Condon factors, relative  $O_2$  vibrational state populations could only be determined for  $v = 6–11$  states, where a monotonic decrease in population was observed. The  $O_2$  vibrational distributions from Smith et al. as well as the NO state-averaged  $O_2$  vibrational distributions obtained in the present study are displayed in Figure 10. The agreement between the two distributions is remarkable, although measurements of the  $O_2(v = 0–5)$  populations resulting from the  $O + NO_2 \rightarrow NO + O_2$  reaction would have provided a more convincing connection, particularly the clear maximum at  $O_2(v = 6–7)$ . Given the large release of potential energy in the exit channel, we have simulated the  $O_2$  vibrational distributions using a sudden approximation, employing a vibrational Franck–Condon analysis.<sup>34,35</sup> Figure 11 shows the results of Franck–Condon simulations of the vibrational distributions for channels 2a and 2b assuming a Morse oscillator for the  $O_2$ . We find excellent agreement with the experimental derived distributions assuming  $O_2$  bond lengths at the time of impulse of 1.451 (2a) and 1.320 Å (2b). The result for the roaming channel (2a) is not surprising as the exoergic  $O + NO_2 \rightarrow NO + O_2$  reaction should have an early transition state in accordance with Polanyi rules.<sup>36</sup>

Previous measurements by Mikhaylichenko et al. revealed that the NO fragment is vibrationally cold, with an overall yield of  $NO(v = 1)$  of  $\leq 0.1$  according to and consistent with the spectator nature of the N–O bond in the reaction.<sup>9</sup> On the basis of our image results, we find that there is a very small yield of channel 2b produced in coincidence with  $NO(v = 1)$  products.

Therefore, given an upper limit of 0.05 for the  $NO(v = 1)$  yield for channel 2b, the  $NO(v = 1)$  yield for channel 2a should be approximately 0.12. Smith et al. reported vibrational populations of NO from the  $O + NO_2$  reaction, distinguishing the nascent NO populations arising from bimolecular reaction from NO produced from  $NO_2$  photodissociation through time-dependent modeling of the data.<sup>32</sup> On the basis of the analysis the authors reported an  $NO(v = 0)$  yield of  $0.82 \pm 0.07$  and an  $NO(v = 1)$  yield of  $0.17 \pm 0.07$  in good agreement with our value of 0.12 for the roaming channel (2a).

The rotational distributions of the  $O_2$  and NO fragments exhibit a clear positive correlation for channel 2a; i.e., as the rotational state of the detected NO increases, the average rotational state of the correlated  $O_2$  increases. Figure 12 (right panel) shows the correlation between the rotational states of the two fragments for this channel. As previously discussed, this was obtained by fitting the  $P(E_T)$  distributions derived from state-selected  $NO(N = 7–33)$  images with Gaussian rotational distributions for correlated  $O_2$ , assumed to be equivalent for each  $O_2$  vibrational band. Linear interpolation of the Gaussian parameters was used to provide continuous  $O_2$  rotational distributions. The intensity of each  $O_2$  rotational distribution was weighted using a Boltzmann rotational temperature of 1300 K for NO. The resulting angular momentum correlation in Figure 12 is shown to be highly constrained. Shown for comparison in the left panel of Figure 12 is the statistical, phase space theory (PST), prediction appropriate for describing loose transition states. PST populates coincident states according to degeneracy, conserving both energy and angular momentum, and not surprisingly fails to capture the strong correlations observed experimentally.<sup>37</sup> A constrained impact parameter impulsive model, used to describe dissociation via tight transition states, would provide a positive correlation between the two fragments. However, such a model is inconsistent with the invariance of the rotational excitation with final product vibrational state. The reduction in the energy available for translational/rotational partitioning with increasing vibrational energy would result in lower rotational energy in both fragments. The weak NO rotation/ $O_2$  vibrational correlation and the weak  $O_2$  rotational/ $O_2$  vibrational correlation observed suggests a wider range of dissociation geometries in the case of channel 2a consistent with the roaming dynamics. Although not discussed explicitly, similar correlations appear to be present in the roaming channel of formaldehyde.

The rotational state correlation is less clear for channel 2b. Although we have fit the state-selected  $P(E_T)$  distributions with a single coincident  $O_2$  rotational distribution to match the broadening of the vibrational structure associated with channel 2a, the lack of vibrational structure for the signal associated with channel 2b makes the rotational correlations for this channel ambiguous. In fact, reasonable fits to the features attributed to channel 2b can be fit nearly as well assuming there is no rotational correlation at all. Such a result is consistent with the formaldehyde system where the rotations of the products are only weakly correlated for the trajectories that access the traditional transition state.<sup>38,39</sup> This was rationalized by recognizing that the rotational energy of each fragment arises from a different mechanism. The  $H_2$  fragment derives from parent vibrational motion with weak exit channel coupling, while the CO fragment rotation is governed by strong torques beyond the transition state.<sup>40</sup> The similarity in NO and  $O_2$  angular momenta in the present case is likely a consequence of the similar fragment B constants.



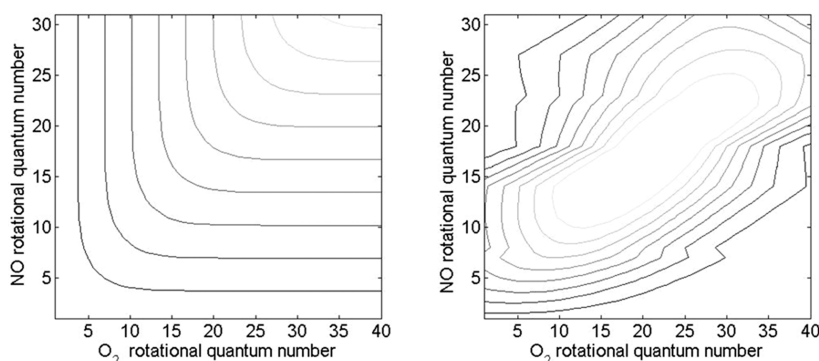


**Figure 12.** Correlated rotational state distributions of the molecular dissociation channel. The left plot shows a simulated statistical angular momentum distribution resulting from  $\text{NO}_3$  ( $T_{\text{rot}} = 20$  K). The right plot shows the experimental angular momentum distribution extracted from the state-selected NO translational energy distributions weighted with a rotational temperature of 1300 K.

Measurement of the  $\nu$ – $J$  correlations in the detected NO fragment may provide additional insight into the dynamics of the two molecular channels.<sup>41,42</sup> In the formaldehyde system the deviation from planarity in roaming trajectories suggests that the resulting NO fragments would exhibit weak  $\nu$ – $J$  correlations. Houston and Kable<sup>17</sup> measured  $\nu$ – $J$  correlations in CO fragments for acetaldehyde dissociation and observed strong  $\nu \perp J$  correlations for high  $J$  CO states but weak  $\nu$ – $J$  correlations for low CO states associated with roaming-type dynamics. Of particular interest are the  $\nu$ – $J$  correlations associated with channel 2b in  $\text{NO}_3$ . A tight three-center transition state should result in  $\nu \perp J$  correlations in NO products. Sensitive measurements of NO  $\nu$ – $J$  correlations have been reported by Cline and co-workers using a two-color (308 + 225 nm) 1 + 1' REMPI detection scheme.<sup>43,44</sup> We are currently pursuing measurements of NO  $\nu$ – $J$  correlations in our laboratory.

## CONCLUSIONS

Correlated product distributions resulting from  $\text{NO}_3$  photolysis through excitation to the  $\text{NO}_3(\text{B } ^2\text{E}')$  state have been measured by velocity map ion imaging. Measurements of the radical channel (1) revealed a statistical distribution of  $\text{O}(^3\text{P}_j)$  fine-structure states and isotropic signal distribution. In addition, total  $P(E_{\text{T}})$  distributions were peaked near zero. All three observations are consistent with barrierless dissociation along the ground potential surface in agreement with the findings of Davis et al.<sup>1</sup>

Two distinct pathways leading to the formation of the molecular products ( $\text{NO} + \text{O}_2$ ) have been identified: channel 2a (>70%), which is comprised of rotationally cold  $\text{NO}(^2\Pi, \nu = 0, 1)$  and vibrationally excited  $\text{O}_2(^3\Sigma_g^-, \nu = 5-10)$ , and channel 2b, which is comprised of rotationally cold  $\text{NO}(^2\Pi, \nu = 0)$  and  $\text{O}_2(^3\Sigma_g^-, \nu = 0-4)$ . The  $\text{O}_2$  excited vibrational state distribution of channel 2a is similar to the distribution resulting from the  $\text{O} + \text{NO}_2$  reaction reported by Smith et al.<sup>32</sup> suggesting the role of roaming type dissociation dynamics.<sup>16</sup> The rotational angular momentum of the two fragments exhibits a strong positive correlation indicating a coupled mechanism for rotational excitation of the fragments in contrast to the formaldehyde system. Efforts toward determination of fragment  $\nu$ – $J$  correlations are currently underway in order to provide additional information on the detailed dynamics of this pathway.

The origin of the second channel (2b) remains largely speculative, although we can identify three possibilities. The first involves a previously unidentified three-center transition along the ground state

potential energy surface. Evidence for this possibility lies in the similarity between the product distributions of this channel and the tight transition state in molecular dissociation of formaldehyde which produces rotationally hot CO coincident with the lower vibrational levels of  $\text{H}_2$ .<sup>15</sup> Efforts to locate a transition state of a relevant energy for the molecular elimination channel in  $\text{NO}_3$ , however, have been unsuccessful. The second possibility involves nonadiabatic interactions with electronic states correlating to excited states of  $\text{O}_2$  in the exit channel or coupling to the dark  $\text{NO}_3(\text{A } ^2\text{E}'')$  state. To our knowledge no theoretical calculations of excited state correlation in the molecular channel have been reported. Excited state correlations to the molecular channel have to our knowledge not been calculated. Finally, we postulate the possibility of a bifurcated roaming potential on the ground state in which both molecular channels arise from intramolecular oxygen atom abstraction from different subsets of geometries. For example, channel 2a may proceed via nearly linear abstraction along the N–O bond axis resulting in low product rotation, while channel 2b may result from a more “sideways” abstraction pathway resulting in fragments with higher product rotational energy. Fragment alignment measurements would also offer valuable insight into this possibility. We also hope this study motivates further theoretical investigation of the ground potential energy surface, as well as the coupling and asymptotic correlations of the excited electronic states.

Finally, we note that crossed molecular beam experiments on the  $\text{NO}_2 + \text{O}(^3\text{P})$  reaction would provide clear evidence for the connection between photochemistry and bimolecular reaction. In particular, the product angular distributions may distinguish between dynamics associated with direct abstraction and  $\text{NO}_3$  complex formation, with the latter perhaps accessing regions of the potential energy surface associated with channel 2b.

## AUTHOR INFORMATION

### Corresponding Author

\*Fax: (979) 845-2971. E-mail: [swnorth@tamu.edu](mailto:swnorth@tamu.edu).

## ACKNOWLEDGMENT

The authors would like to thank Arthur Suits, Wolfgang Eisfeld, and H. Floyd Davis for helpful discussions regarding  $\text{NO}_3$ . We would also like to thank Justine Geidosch for her help in developing the synthesis of  $\text{N}_2\text{O}_5$ . Support for this project was provided by the Robert A. Welch Foundation (A-1405).



## ■ REFERENCES

- (1) Davis, H. F.; Kim, B. S.; Johnston, H. S.; Lee, Y. T. *J. Phys. Chem.* **1993**, *97*, 2172.
- (2) Magnotta, F.; Johnston, H. S. *Geophys. Res. Lett.* **1980**, *7*, 769.
- (3) Orlando, J. J.; Tyndall, G. S.; Moortgat, G. K.; Calvert, J. G. *J. Phys. Chem.* **1993**, *97*, 10996.
- (4) Davis, H. F.; Ionov, P. I.; Ionov, S. I.; Wittig, C. *Chem. Phys. Lett.* **1993**, *215*, 214.
- (5) Johnston, H. S.; Davis, H. F.; Lee, Y. T. *J. Phys. Chem.* **1996**, *100*, 4713.
- (6) Stanton, J. F.; Okumura, M. *Phys. Chem. Chem. Phys.* **2009**, *11*, 4742.
- (7) Marinelli, W. J.; Swanson, D. M.; Johnston, H. S. *J. Chem. Phys.* **1982**, *76*, 2864.
- (8) Nelson, H. H.; Pasternack, L.; McDonald, J. R. *J. Chem. Phys.* **1983**, *79*, 4279.
- (9) Mikhaylichenko, K.; Riehn, C.; Valachovic, L.; Sanov, A.; Wittig, C. *J. Chem. Phys.* **1996**, *105*, 6807.
- (10) Eisfeld, W.; Morokuma, K. *J. Chem. Phys.* **2001**, *114*, 9430.
- (11) Grubb, M. P.; Warter, M. L.; Suits, A. G.; North, S. W. *J. Phys. Chem. Lett.* **2010**, *1*, 2455.
- (12) Vanzee, R. D.; Foltz, M. F.; Moore, C. B. *J. Chem. Phys.* **1993**, *99*, 1664.
- (13) Townsend, D.; Lahankar, S. A.; Lee, S. K.; Chambreau, S. D.; Suits, A. G.; Zhang, X.; Rheinecker, J.; Harding, L. B.; Bowman, J. M. *Science* **2004**, *306*, 1158.
- (14) Suits, A. G. *Acc. Chem. Res.* **2008**, *41*, 873.
- (15) Lahankar, S. A.; Chambreau, S. D.; Townsend, D.; Suits, F.; Farnum, J.; Zhang, X. B.; Bowman, J. M.; Suits, A. G. *J. Chem. Phys.* **2006**, *125*.
- (16) Christoffel, K. M.; Bowman, J. M. *J. Phys. Chem. A* **2009**, *113*, 4138.
- (17) Houston, P. L.; Kable, S. H. *Proc. Natl. Acad. Sci. U.S.A.* **2006**, *103*, 16079.
- (18) Goncharov, V.; Herath, N.; Suits, A. G. *J. Phys. Chem. A* **2008**, *112*, 9423.
- (19) Harding, L. B.; Klippenstein, S. J. *J. Phys. Chem. Lett.* **2010**, *1*, 3016.
- (20) Kim, H.; Park, J.; Niday, T. C.; North, S. W. *J. Chem. Phys.* **2005**, *123*, No. 174303.
- (21) Dooley, K. S.; Grubb, M. P.; Geidosch, J.; van Beek, M. A.; Groenenboom, G. C.; North, S. W. *Phys. Chem. Chem. Phys.* **2009**, *11*, 4770.
- (22) Kim, H.; Dooley, K. S.; Johnson, E. R.; North, S. W. *Rev. Sci. Instrum.* **2005**, *76*, No. 124101.
- (23) Davidson, J. A.; Viggiano, A. A.; Howard, C. J.; Dotan, I.; Fehsenfeld, F. C.; Albritton, D. L.; Ferguson, E. E. *J. Chem. Phys.* **1978**, *68*, 2085.
- (24) Luque, J. LIFBASE 2.0.
- (25) Roberts, G. M.; Nixon, J. L.; Lecointre, J.; Wrede, E.; Verlet, J. R. *Rev. Sci. Instrum.* **2009**, *80*, No. 053104.
- (26) Baer, T. H.; William, L. *Unimolecular Reaction Dynamics: Theory and Experiments*; Oxford University Press: Oxford, 1996.
- (27) Muckerman, J. T. *J. Phys. Chem.* **1989**, *93*, 179.
- (28) Ben-Shaul, A.; Levine, R. D.; Bernstein, R. B. *J. Chem. Phys.* **1974**, *61*, 4937.
- (29) Due to the close proximity of the NO rotational lines, the experimental images shown here are not scanned over the Doppler profile, giving rise to observed anisotropy. Careful measurements utilizing a full Doppler scan were taken at more isolated lines which show the images are inherently isotropic.
- (30) Ahmed, M. P.; Peterka, D. S.; Suits, A. G. In *Atomic and Molecular Beams: The State of the Art 2000*; Campargue, R., Ed.; Springer: New York, 2001; p 343.
- (31) Brown, J. M.; Cole, A. R. H.; Honey, F. R. *Mol. Phys.* **1972**, *23*, 287.
- (32) Smith, I. W. M.; Tuckett, R. P.; Whitham, C. J. *Chem. Phys. Lett.* **1992**, *200*, 615.
- (33) Troe, J. *Ber. Bunsen-Ges. Phys. Chem.* **1969**, *73*, 906.
- (34) Berry, M. J. *Chem. Phys. Lett.* **1974**, *27*, 73.
- (35) Schinke, R. *Photodissociation Dynamics*; Cambridge University Press: Cambridge, 1993.
- (36) Polanyi, J. C. *Acc. Chem. Res.* **1972**, *5*, 161.
- (37) The low parent rotational temperature requires that the difference in angular momentum between the fragments is balanced by orbital angular momentum.<sup>35</sup> Constraining the PST calculation with an exit impact parameter to 0.2 Å provides an upper limit to the orbital angular momentum and reproduces the experimental correlation.
- (38) Debarre, D.; Lefebvre, M.; Pealat, M.; Taran, J. P. E.; Bamford, D. J.; Moore, C. B. *J. Chem. Phys.* **1985**, *83*, 4476.
- (39) Butenhoff, T. J.; Carleton, K. L.; Chuang, M. C.; Moore, C. B. *J. Chem. Soc., Faraday Trans. 2* **1989**, *85*, 1155.
- (40) Schinke, R. *J. Chem. Phys.* **1986**, *84*, 1487.
- (41) Hall, G. E.; Sivakumar, N.; Houston, P. L.; Burak, I. *Phys. Rev. Lett.* **1986**, *56*, 1671.
- (42) North, S. W.; Hall, G. E. *J. Chem. Phys.* **1996**, *104*, 1864.
- (43) Uberna, R.; Hinchliffe, R. D.; Cline, J. I. *J. Chem. Phys.* **1996**, *105*, 9847.
- (44) Nestorov, V. K.; Cline, J. I. *J. Chem. Phys.* **1999**, *111*, 5287.